Applied Acoustics 181 (2021) 108120

Contents lists available at ScienceDirect

Applied Acoustics

journal homepage: www.elsevier.com/locate/apacoust

Geometric optimization of dielectric elastomer electrodes for dynamic applications

Emil Garnell [a,*], Bekir Aksoy [b], Corinne Rouby [a], Herbert Shea [b], Olivier Doaré [a]

[a] IMSIA, CNRS, ENSTA Paris, EDF, CEA, Institut Polytechnique de Paris, France
[b] LMTS, École Polytechnique Fédérale de Lausanne, Switzerland

ARTICLE INFO

Article history:
Received 4 November 2020
Received in revised form 22 March 2021
Accepted 14 April 2021
Available online 14 May 2021

Keywords:
Dielectric elastomer
Modal analysis
Parametric optimization

ABSTRACT

Dielectric elastomers are soft actuators, made of an elastomer membrane sandwiched by compliant electrodes. Because of their high energy density and quick response, they are well suited for dynamic applications such as loudspeakers. Thanks to progress in the manufacturing process of dielectric elastomer actuators, the electrode shape can be patterned to very diverse shapes. In this study, we focus on the relation between the electrode shape and the dynamical and acoustical behavior of a dielectric elastomer loudspeaker. By using a finite element model of the loudspeaker, an optimization algorithm is set up to compute optimal electrode shapes according to chosen objectives, such as maximizing or minimizing the contribution of an eigenmode to the radiated sound. The optimal designs are then tested experimentally, and the efficiency of the optimization procedure is assessed. It is shown that the frequency response of dielectric elastomer loudspeakers can be tuned by optimizing the shape of the electrodes, and simulations suggest that the directivity can also be controlled. Finally, perspectives of the proposed optimization method are briefly discussed.

1. Introduction

Dielectric elastomers (DEs) are active materials capable of large electrically-triggered deformations (up to 500% area strain [1,2]). They consist of a soft elastomer membrane sandwiched between compliant and stretchable electrodes, forming a deformable capacitor. When a high voltage is applied between the electrodes, an electrostatic pressure squeezes the membrane whose area therefore increases [3], see Fig. 1. This mechanism is very fast, and can be effective for frequencies up to 16 kHz [4] especially if silicone is used as the membrane material [5]. DEs have been investigated for a wide range of applications including soft robotics [6,7], artificial muscles [8], micro-pumps [9,10], vibration absorbers [11], and loudspeakers [12].

As explained in Fig. 1 the membrane is compressed by the electrostatic pressure only between the electrodes, and the rest of the membrane is passive. It is therefore possible to tune the actuation by patterning the electrode, and choosing cleverly where electrodes should be deposited.

This idea has been exploited by several research groups, for very diverse objectives. Conn et al. [13] patterned the electrodes on a cone DE actuator to generate a rotating motion during actuation. Zou et al. [14] studied the influence of the electrode shape on the static deformation of an inflated DE membrane. Langham et al. [15] analysed the buckling of DE structures, and in particular the influence of the electrode shape on the type of buckling. They showed that the buckling wavelength can be controlled by the aspect ratio of an annular electrode on a circular membrane.

By patterning multiple independently addressable electrodes on both sides of the elastomer membrane, different actuation shapes can be obtained. This principle has been used for instance to manufacture rotating motors [16,17] by using three or four independent electrodes, and to make reconfigurable surfaces [18].

Patterned electrodes have also been widely investigated for soft grippers using the electro-adhesion principle [19]. Strong fringing fields are obtained by using several electrodes polarized with opposite voltages. Shintake et al. [20] used electrode patterning techniques for DE actuators to combine electro-adhesion and actuator capabilities. Similarly, Gao et al. [21] used patterned electrodes to actuate a soft gripper at resonance to improve the release. A prototype of a wall-climbing robot has been developed by Gu et al., using a DE actuator and electro-adhesion obtained with patterned electrodes [6].

* Corresponding author. Olivier Doaré, ENSTA Paris, 828 Boulevard des Maréchaux, 91120 Palaiseau, France
E-mail address: olivier.doare@ensta-paris.fr (O. Doaré).

https://doi.org/10.1016/j.apacoust.2021.108120
0003-682X/

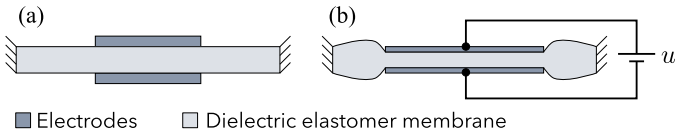

Fig. 1. Principle of dielectric elastomer actuators. (a) Initial state. (b) Deformed state, when a high voltage u is applied.

The above-mentioned applications of electrode patterning for DE actuators are for static [20,19], or dynamic cases [6], in which the kinetic energy of the DEA can be neglected compared either to the kinetic energy of a heavier biasing load, or to the potential elastic energy of biasing elements. However, because of their quick response, DE actuators are also used in high frequency applications where the DE membrane itself exhibits a modal behavior [4,22,23]. Few studies focus on the relation between the electrode shape and the dynamic behavior of DE structures.

For other electro-active materials, such as piezo-electric materials for example, the optimal placement of the electrodes for vibration control has been investigated [24]. Such studies are closely related to the modeshapes analysis of the structure, as playing on the location of the excitation will increase or decrease the modal forces on the different eigenmodes. This idea has been exploited to perform modal control on flat loudspeakers: Doaré et al. [25] used piezoelectric patches to cancel the modal forces of undesirables modes, and Jiang et al. [26] optimized the location of several voice-coils to minimize the contribution of unwanted modes.

In the present study, we focus on a given DE actuator geometry, namely an inflated DE loudspeaker (see Fig. 2). When the DE membrane is inflated, the increase in area when the high voltage is applied is converted to an increase of volume of the inflated balloon [27,22]. If an oscillating voltage is applied, an acoustic volume source is obtained. This configuration has been widely studied for acoustic applications [28,4], and we have previously developed a numerical model to compute its sound radiation [29,30].

Here, we show that the shape of the electrodes can be tuned to adjust the acoustic frequency response of the structure, by playing on the modal forces. A finite element model is used to obtain a modal description of the structure, which is then fed into a global optimization algorithm, to improve a simple optimization objective: maximizing or minimizing the contribution of a given eigenmode to the acoustic radiation of the loudspeaker.

The article is organized as follows: first a quick overview of the finite element model of the DE loudspeaker is presented, and the optimization algorithm is introduced. A prototype with the optimal electrodes is then manufactured, and the process to deposit the patterned electrodes is presented in Section 3. The effect of the optimization on the radiated acoustic pressure is finally analysed in the results Section 4, and perspectives are discussed.

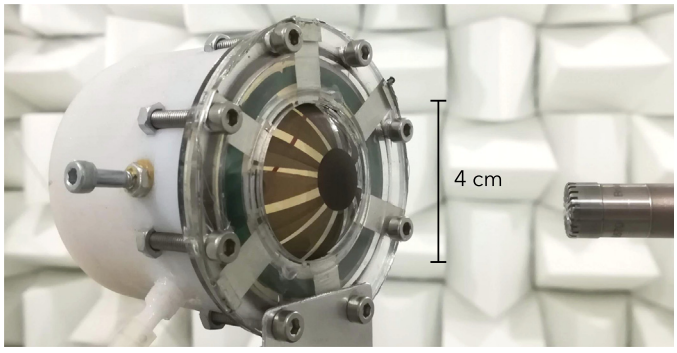

Fig. 2. Picture of an inflated DE loudspeaker prototype during acoustical measurements in the anechoic chamber of ENSTA.

2. Optimization procedure

The optimization procedure presented in this article is based on a finite element model of the inflated DE loudspeaker shown in Fig. 2, which is described in details in [29,30]. In the following only a short overview of this model is given, to provide the key elements which are needed for the optimization.

2.1. Model of the inflated DE loudspeaker

To simplify the notations in the whole article, all variables are non-dimensional.

We consider an elastomer membrane coated by electrodes on a portion of its surface described by the electrode indicative function Γ, which equals unity when an electrode is present, and zero otherwise. The membrane is then placed over a closed cavity, pre-stretched, and inflated with a static pressure (see Figs. 2 and 3). A high voltage u is applied between the electrodes to vibrate the membrane and radiate sound.

To study this setup, a reference configuration is defined, where the membrane is flat and at rest, and parametrized by the radius R (see Fig. 3(a)). When it deforms, the membrane Σ is parametrized by the coordinates $\boldsymbol{x}(R) = [r(R), z(R)]$. The principal stretches are denoted λ_1 and λ_2 (see Fig. 3(b)). The pressure inside the cavity is denoted p_i, and the radiated pressure p_e.

The membrane behavior is modeled by a hyper-elastic Gent law [31], and the electromechanical coupling appears as an added stress ($\sigma_{\text{Max}} = \epsilon u^2/h^2$ where ϵ is the elastomer dielectric permittivity) in the constitutive relations relating the stress to the deformation of the membrane [3]. Note that the electrostatic stress is proportional to the voltage squared, which creates a large non-linearity. For loudspeaker applications, a linear relation between the input signal and the radiated pressure is desired, to avoid harmonic distortion. In order to obtain a linear excitation, the loudspeaker is driven with the following voltage [28]:

$$u(t) = U\sqrt{1 + w(t)}, \text{ with } |w(t)| < 1, \tag{1}$$

where U is a static bias voltage, and w the audio signal. This implies that electrostatic stress is proportional to $w(t)$.

The coupling between the membrane vibrations and acoustics needs to be taken into account because the membrane is very thin, and the added mass effect which arises when the membrane vibrates the surrounding air is strong [30]. To this aim, a fully coupled model of the membrane dynamics and acoustics inside and outside of the cavity is setup in the open source finite element software FreeFEM [32]. The mesh density is 12 elements per flexural or

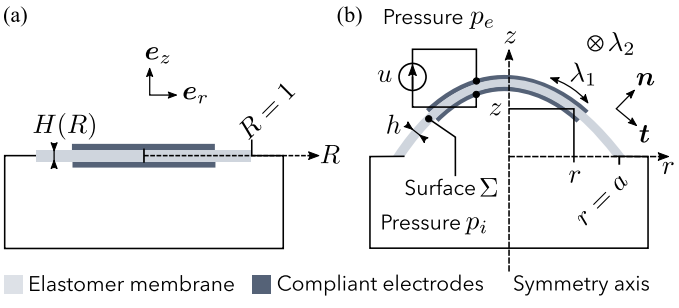

Fig. 3. Model of an inflated DE membrane, and definition of the needed variables. (a) Reference configuration: the membrane is flat and at rest. Variables in the reference configuration are written with capital letters. (b) Deformed configuration: the membrane is inflated with the pressure p_i and a high voltage u is applied.

acoustic wavelength (respectively for the membrane and for acoustics) at the highest studied frequency, with a conforming mesh at the interface. The free-field radiation boundary condition is implemented by using perfectly matched layers (PMLs) [33]. The system of coupled governing equations can finally be written in the following form after discretization by finite elements:

$$(-\omega^2\boldsymbol{M}+\boldsymbol{K})\boldsymbol{X}=\boldsymbol{F}, \tag{2}$$

where ω is the frequency of the electrical excitation, $\boldsymbol{X}=[\boldsymbol{x}, q_i, q_e]$ is the vector gathering all unknowns, where $q_i=p_i/\omega^2$ and $q_e=p_e/\omega^2$ are the fluid displacement potentials. $\boldsymbol{M}$ and $\boldsymbol{K}$ are the total mass and stiffness matrices, and $\boldsymbol{F}$ the force vector, generated by the electrostatic stress. Two modelling choices (frequency-independent PMLs and hysteretic damping) imply that the obtained mass and stiffness matrices $\boldsymbol{M}$ and $\boldsymbol{K}$ are frequency-independent. Without the forcing term $\boldsymbol{F}$, eq. 2 is therefore a linear eigenvalue problem, which can be solved by standard eigenvalue solvers.

Modal expansions of the displacement of the membrane $\boldsymbol{x}$, and of the radiated pressure p_e are obtained:

$$\boldsymbol{x}=\sum_n \frac{F_n}{\omega_n^2-\omega^2}\boldsymbol{\Psi}_{\mathrm{n}}^{\mathrm{x}},\ p_e=\sum_{\boldsymbol{n}} \omega^2\frac{F_n}{\omega_n^2-\omega^2}\Psi_n^e, \tag{3}$$

where F_n is the modal force on mode n, ω_n the eigenfrequency, $\boldsymbol{\Psi}_n^x$ and Ψ_n^e the parts of the coupled modeshape n containing the structural and exterior acoustics degrees of freedom respectively.

We are interested in the pressure at a given receiver position $\boldsymbol{x}_r$, so by defining the modal participation factor $A_n=F_n\Psi_n^e(\boldsymbol{x}_r)$, the pressure radiated at the receiver location reads:

$$p_e(\boldsymbol{x}_r)=\sum_n \omega^2\frac{A_n}{\omega_n^2-\omega^2}. \tag{4}$$

The contribution of mode n to the radiated pressure at $\boldsymbol{x}_r$ is thus proportional to A_n.

2.2. Definition of the optimization problem

In the present study, we aim at optimizing the shape of the electrode to improve objective functions which will be defined in Section 2.3. The prototype is axisymmetric, and only axisymmetric electrodes will be considered in the following. The electrode shape is thus parametrized by a set of radii, defined in Fig. 4.

For the electrode shown in Fig. 4(b), the electrode indicative function Γ is defined as follows:

$$\Gamma(R)=\begin{cases}1 & \text{for } \mathrm{R}\leqslant \mathrm{R}_1 \text{ or } \mathrm{R}_2<\mathrm{R}\leqslant \mathrm{R}_3.\\ 0 & \text{otherwise.}\end{cases} \tag{5}$$

and the electrode radii can vary in the range:

$$R_{i-1}<R_i\leqslant R_{i+1}. \tag{6}$$

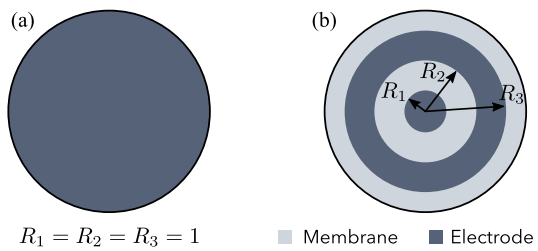

Fig. 4. Definition of the optimized parameters: the non-dimensional radii R_i of the different electrode rings. Here, an electrode with 3 radii is shown. (a) Initial electrode (where the second electrode between R_2 and R_3 is infinitely narrow). (b) Optimized electrode.

In the following, the radii of the electrodes will be optimized to minimize the cost functions introduced in the following Section 2.3. The definition of the optimization parameters given in Fig. 4 is unpractical, as it defines a bounded optimization problem, where the bounds for one parameter depends on the values of the other parameters. In order to overcome this difficulty, relative radii are defined as:

$$\check{R}_i=\frac{R_i}{R_{i+1}} \text{ for i} < \mathrm{N_R},\quad \check{R}_i=R_i \quad \text{for} \quad \mathrm{i}=\mathrm{N_R}, \tag{7}$$

where N_R is the number of optimized radii. All $\check{R}_i$ vary between 0 and 1. We define for the following a vector $\check{\boldsymbol{R}}$ containing all the optimized radii $\check{R}_i$: $\check{R}=[\check{R}_1,\check{R}_2,\check{R}_3,\ldots]$.

2.3. Objective functions

In order to validate the optimization method, simple objective functions will be used. The contribution of the second membrane mode to the radiated pressure will be either maximized or minimized. These goals have been chosen because they yield clear results for relatively simple electrode shapes, as it will be shown in Section 4.

To maximize the contribution of the second mode to the total sound radiation compared to the other modes, we define from Eq. 4 the following objective function which should be minimized [34]:

$$I=\frac{\sum_{n\neq 2}|A_n|^2}{|A_2|^2}. \tag{8}$$

If on the other hand the radiation of the second mode should be minimized, the following objective function should be used:

$$J=\frac{|A_2|^2}{\sum_{n\neq 2}|A_n|^2}. \tag{9}$$

2.4. Optimization algorithm

The general principle of the optimization algorithm is that the time-consuming operations, namely computing the modal parameters (eigenfrequencies, eigenmodes and modal loss factors) should be performed only once. To this end, we make the following assumption:

Assumption 1. The electrodes have a negligible influence on the eigenfrequencies, modal damping and modeshapes of the inflated DE membrane.

This presumes that the mass and stiffness of the electrodes are negligible compared to those of the membrane. As a result, the modal parameters do not change when the electrode shape is varied during the optimization process. The electrode shape only changes the modal forces, which can be computed quickly using the following formula [29]:

$$F_n(\check{\mathbf{R}})=\int_0^1 \frac{\Gamma_{\mathbf{R}}}{h}\left(r\lambda_2\frac{\partial\boldsymbol{\Psi}_n^x}{\partial R}\cdot\boldsymbol{t}+\lambda_1\boldsymbol{\Psi}_n^x\cdot\boldsymbol{e}_r\right)\lambda_1\lambda_2\mathrm{d}R, \tag{10}$$

Inserting this expression in the definition of A_n yields:

$$A_n(\check{\mathbf{R}})=\int_0^1 g_n(R)\Gamma_{\check{R}}(R)\mathrm{d}R. \tag{11}$$

where we have defined g_n as:

$$g_n(R)=\Psi_n^e(\boldsymbol{x}_r)\frac{1}{h}\left(r\lambda_2\frac{\partial\boldsymbol{\Psi}_n^x}{\partial R}\cdot\boldsymbol{t}+\lambda_1\boldsymbol{\Psi}_n^x\cdot\boldsymbol{e}_r\right)\lambda_1\lambda_2. \tag{12}$$

All the terms appearing in Eq. (12) are independent of the electrode shape, so g_n only needs to be computed once. The cost functions I and J defined by Eqs. (8) and (9) depend only on the modal participation factors $A_n(\check{\mathbf{R}})$, which can be computed quickly as Eq. (11) is only a summation.

The optimization is performed as follows, and is described in Fig. 5:

1. Compute the modal parameters using the model.
2. Build a function that returns the cost as a function of the electrode radii.
3. Feed this function into a non-linear global optimization routine.

In the present study we used the *MultiStart* algorithm from the Matlab Global Optimization Toolbox. This algorithm runs a local minimization on a randomly chosen set of starting points, and the smallest minimum retained at the end. There is no guaranty that the obtained minimum is the global minimum, but the more starting points are used, the higher is the chance to find the global minimum. The optimization has been run with increasing number of starting points, and when the obtained minimum was found to be independent of the number of starting points it is considered to be a good estimation of the global minimum. Finally 10^3 starting points are used.

The optimization process described above yields as a result the optimal radii of the electrodes. The results obtained with the two cost functions I and J are given in Table 1.

The finite element model can then be used to compute the frequency response of the loudspeaker with these optimal electrodes, which provides a first validation of the optimization procedure. To validate further the proposed algorithm, prototypes with the optimal electrodes are manufactured, and their frequency response is measured.

3. Manufacturing process

In this section, the manufacturing process to build DE loudspeaker prototypes with optimal electrodes is described. First, general design considerations on the electrodes connections to the electrical supply are discussed, and the process to deposit the electrodes is then presented.

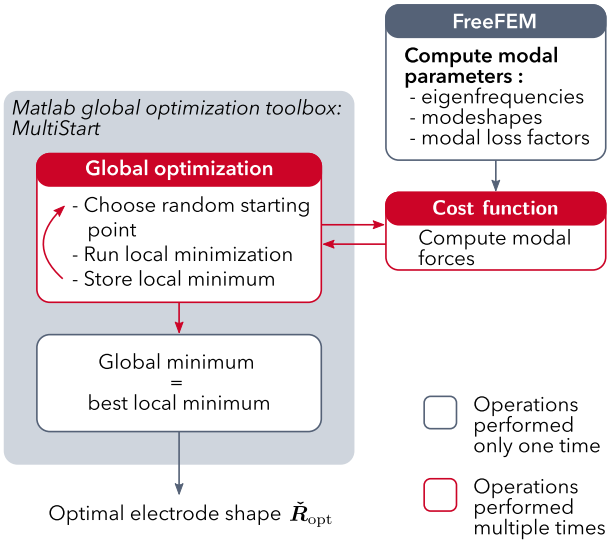

Fig. 5. Flowchart of the optimization procedure.

3.1. Electrode design

As explained in Section 2.2, the electrode consists in several concentric rings. However, these different rings must be connected to the electrical supply, so connections need to be designed and added.

The electrostatic pressure which deforms the membrane applies only on areas of the membrane which are covered on both sides by electrodes. If an electrode is present only on one side, or if there is no electrode on neither sides, no electrostatic pressure applies. This can be exploited to design the connections, by extending the electrodes while making sure that they are overlapping only in the desired areas.

The chosen electrode design is shown in Fig. 6, where the desired active area is a disk. To connect the disk to the power supply, six radial electrodes are added between the disk and the frame, where aluminum tape is placed in contact with the electrode. The connections of the top and bottom electrodes are rotated by 30°, so that they are not superimposed. This way, electrodes are present on both sides of the membrane only in the central disk, which is the desired active area.

The electrodes are not perfectly conductive [35], so the connections add electrical resistance to the electrical circuit, which reduces the bandwidth in which the actuator can operate. The resistance created by the electrode connections is minimized in the designed proposed in Fig. 6 by using all the available membrane area as connections: by increasing the number and the width of the connections, the connection resistance decreases. With the chosen electrode design and a surface resistivity of 10 kΩ/sq, the electrical cutting frequency lies around $1/2\pi R_e C \approx 10$ kHz, where R_e and C are the lumped resistance and capacitance of the membrane.

The system should remain as axisymmetric as possible, which is why we decided to use many small connections instead of a large one.

3.2. Pad-printing the electrodes

To deposit with good accuracy the electrodes on the dielectric membrane, the pad-printing method proposed by Rosset et al. [36] has been used. The dielectric membrane is a 50 μm thick silicone film (Silpuran Film 2030 from Wacker Chemie AG). A small prestretch of 1.1 is applied to keep the membrane flat during the fabrication. The electrodes are made of carbon-black (Ketjenblack EC-600JD from Akzo Nobel N.V) loaded silicone (Silbione LSR 4305 from Elkem Silicones), which yields compliant and durable electrodes [36].

The pad-printing process is described by the schematics in Fig. 7. First, a cliché is manufactured. It consists in a metal plate where a disk is etched. The disk diameter corresponds to the largest electrode diameter that can be deposited (40 mm in our case). When the ink reservoir of the pad-printer is slid over the cliché, ink stays in the etched area, and will be picked up by the soft silicone stamp.

To pattern the electrode, a thin Mylar film is laser-cut to form a mask corresponding to the shape of the electrode. It is placed on the membrane before the pad applies the ink. The electrostatic adhesion between the mylar and the silicone membrane prevents the ink from penetrating under the mask.

Pictures of the membranes with the three different types of electrodes defined in Table 1 which have been manufactured at the LMTS by the method described above are shown in Fig. 8. The pad printing process yields precise electrodes, with clean edges.

Table 1
Optimal electrode radii, obtained for the two cost functions. In the initial design the electrode covers the whole membrane.

No	Goal	Cost function	Optimal radii $\boldsymbol{R}_{opt}$	Electrode shape
1	Initial design	–	[1, 1, 1]	
2	Max. mode 2	I	[0, 0.41, 0.73]	
3	Min. mode 2	J	[0.32, 1, 1]	

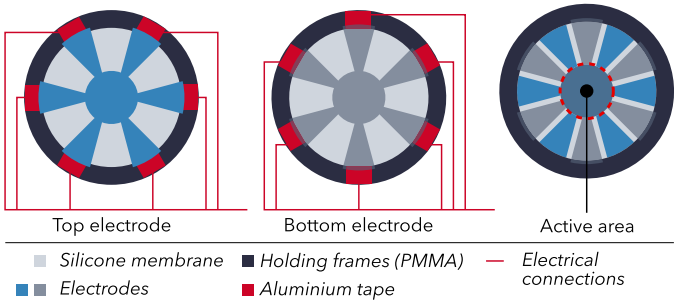

Fig. 6. Design of the electrodes and of the electrical connections. The active area is enclosed by the red dashed circle.

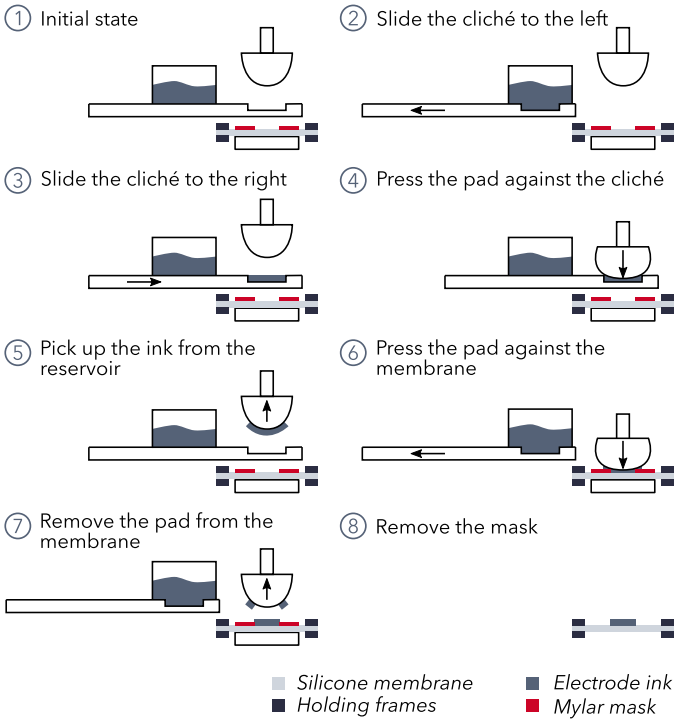

Fig. 7. Pad-printing procedure used to apply the soft conductive electrodes. The steps 1-8 are then repeated on the other side of the membrane to apply the second electrode.

The thickness of the electrodes (and consequently their surface resistivity) can be controlled by repeating the pad-printing (stages 1 to 7 in Fig. 7). With a single printing, the obtained electrodes are approximately 3 µm-thick, which is small compared to the thickness of the membrane (this estimation is obtained from the mass added during the pad-printing process).

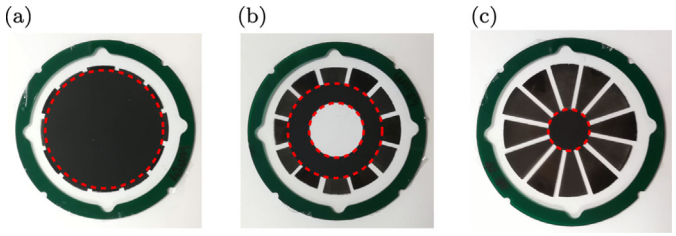

Fig. 8. Manufactured membranes with the three electrode shapes defined in 1. The active areas are enclosed by the red dashed circles. (a) Electrode 1: initial design. (b) Electrode 2: maximize radiation of mode 2. (c) Electrode 3: minimize radiation of mode 2.

4. Results and discussion

4.1. Experimental validation of the optimal designs

Given the chosen cost functions I and J, the electrode shape has been optimized and resulted in the electrodes defined in Table 1. The optimal electrodes have been manufactured following the process described in the previous Section 2. In the present section, the sound radiation obtained with the three electrode designs is analysed to assess the efficiency of the optimization process.

All acoustical measurements have been performed in the anechoic chamber of ENSTA, which is $3 \times 3 \times 3$ m^3 large and specified down to 120 Hz. The pressure is measured on axis at 1 m, and the transfer function between the electrical excitation w and the radiated pressure is obtained by the exponential swept sine method [37].

The measured transfer functions are plotted in Fig. 9 together with the results of the model, for the three electrode designs.

The global shape of the radiated pressure is the same for the three electrode shapes: at low frequencies (500Hz 3000 Hz), the response is dominated by the membrane modes. At high frequencies (above 3 kHz), large peaks can be observed. They are caused by the acoustic resonances inside the cavity on which the membrane is inflated [30] (see Fig. 2 and 3).

When the electrode occupies the whole membrane (electrode 1), the acoustic radiation is dominated by the second membrane mode, at 750 Hz. When the radiation of this second mode is maximized (electrode 2), the difference between the peak level of mode 2 and of the neighboring modes increases further. In particular, the radiation of the third mode around 1000 Hz has decreased. Moreover, the overall radiated level decreased, as a consequence of a smaller electrode area (36% of the initial electrode area) which reduces the electrostatic excitation.

The third electrode design also succeeds is satisfying its goal: minimizing the radiation of the second mode. The amplitude of the second peak in Fig. 9(c) is similar to the surrounding modes 1, 3, 4 and 5. Compared to the initial design Fig. 9(a), the difference in amplitude between the second peak and the neighboring peaks has decreased by 15 dB. Of course, the electrode area is even smaller than electrode 2 (10% of the initial area, see Fig. 8), so the radiated level is even lower.

Although the expected improvements are observed, none of the optimizations has succeeded in reducing the cost function to zero: the other modes still contribute to the radiation in Fig. 9(b), and mode 2 still radiates in Fig. 9(c). This can be understood by looking at Fig. 10, where the functions g_n defined by Eq. 12 are plotted for the first 4 modes. We recall that the contribution of a given mode n to the radiated pressure is proportional to A_n, which is the integral

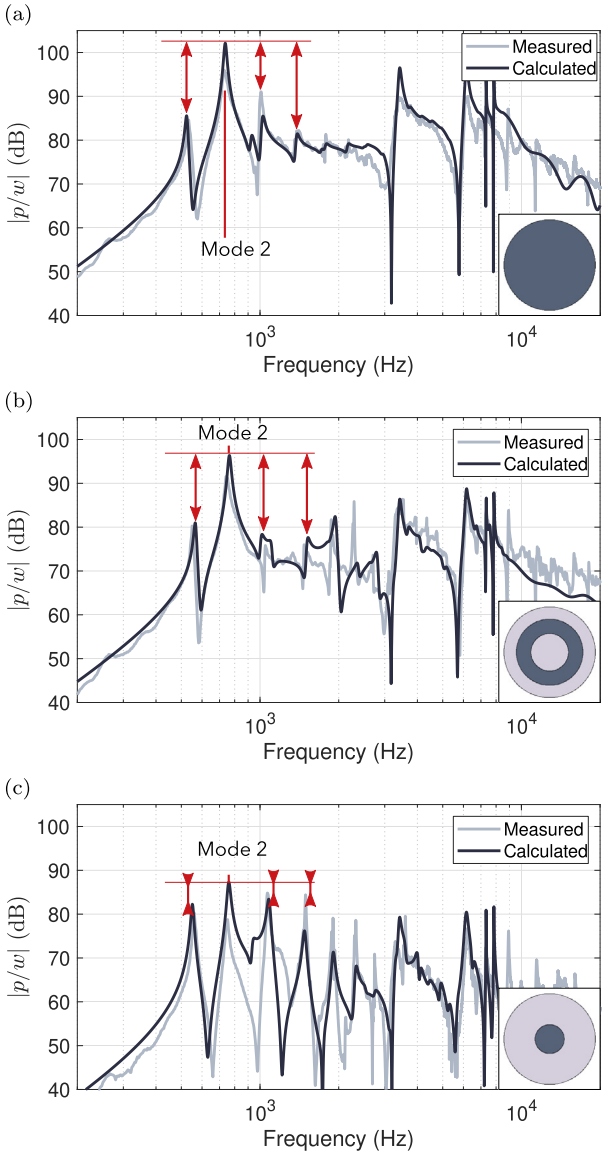

Fig. 9. Transfer function between the radiated acoustic pressure at 1m on axis and the excitation signal. The electrode shape is shown in the bottom right corner. (a) Electrode 1. (b) Electrode 2. (c) Electrode 3.

of g_n on portions of the membrane where an electrode is present on both sides (see Eq. 11).

Fig. 10 shows that g_2 is always positive, so the integral of g_2 times the indicative function of the electrode Γ cannot be cancelled, except if there is no electrode. As a consequence, whatever the electrode shape, mode 2 will contribute to the sound radiation.

Fig. 10 also helps to interpret the optimal electrode shapes: for example when the radiation of the second mode is maximized, the optimal electrode is a ring around radius $R \approx 0.6$. This corresponds to a radius where g_3 and g_4 change signs, so the integral of these functions on this ring will be very small. At the same time, $R \approx 0.6$ corresponds to electrode locations where g_2 is very large.

4.2. Discussion

In the previous section, we showed that the optimization is limited by the shape of the modal participation functions g_n (see

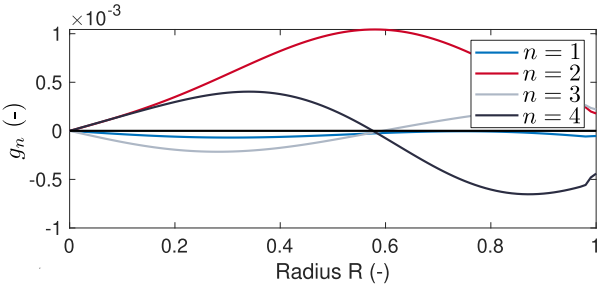

Fig. 10. Modal participation factor as a function of the membrane radius for the first four modes.

Fig. 10). The contribution of the second mode cannot be reduced to zero since the function g_2 is positive for all radii.

One option to further decrease the contribution of mode 2 to the sound radiation could be to excite one of the electrode rings out of phase. Indeed, this is equivalent to setting the electrode indicative function to 1 on the electrodes actuated in phase, and to -1 on the electrodes actuated out of phase.

To test this idea, we perform an optimization of the cost function J, for an electrode with 5 radii (three rings), and set the second ring out of phase (see Fig. 11(b)). This electrode is denoted electrode 4.

The numerical results presented in Fig. 11 show that the optimization with the second electrode out of phase succeeds in completely canceling the contribution of mode 2 to sound radiation, which is now dominated by the contributions of modes 3 and 4, around 1 kHz.

Possible applications of this kind of optimizations may be to control the directivity of DE loudspeakers. Indeed, each membrane mode has a specific directivity pattern, so by controlling which mode dominates the frequency response the directivity can be controlled.

For example, for the optimization presented in Fig. 11, the mode 2 has a more omnidirectional radiation pattern than higher order modes. As a consequence, decreasing the contribution of mode 2 to the radiation increases the near-field directionality of the loudspeaker, as shown in Fig. 12. This is particularly visible at high frequencies, because the loudspeaker is acoustically compact at low frequencies below approximately 3 kHz (its size is small compared to the acoustical wavelength) and radiates as a monopole. Near field directivity control may be useful for headphones applications for example.

This simple example highlights the wide range of tuning possibilities which is opened by electrode shape optimization.

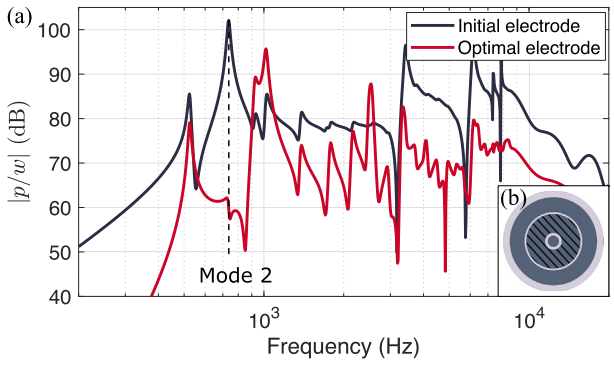

Fig. 11. (a) Computed radiation of the DE loudspeaker with electrode 4, for cost function J. (b) Optimal electrode shape. The second electrode ring (hatched) is driven out of phase of the two other rings.

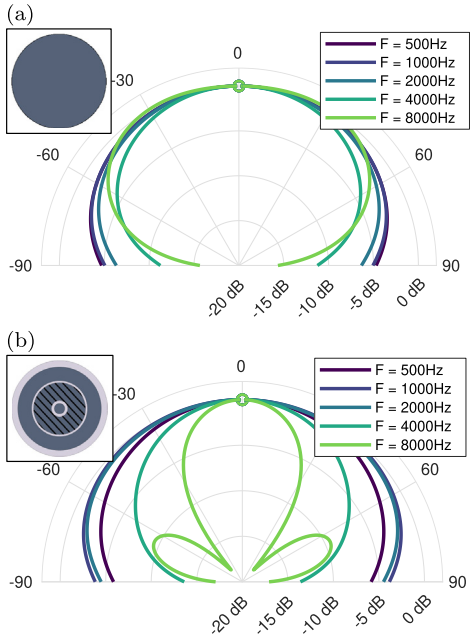

Fig. 12. Near field directivity of the inflated DE loudspeaker, computed by the finite element model on a circle of 5 cm diameter centered on the membrane, and normalized by the level on axis. (a) Initial design, with electrode 1 (see 1). (b) Optimal electrode obtained when the second electrode ring is actuated out of phase, shown in 11(b).

5. Conclusion

In this article, we investigated the influence of the electrode shape on the dynamics of dielectric elastomer actuators. We focused on an inflated DE loudspeaker to demonstrate that the electrode can be optimized to tune the dynamic behavior.

An optimization method based on a finite element model of the loudspeaker has been presented, and two objective functions have been considered, aiming at either increasing or decreasing the contribution of the second membrane mode to the sound radiation. It has been shown experimentally that the optimization succeeds in improving the considered objectives.

In the present article we focused on simple cost functions which yield clear and easily interpreted results, and demonstrated that the sound radiation can be tuned by adjusting the electrode shape. More acoustically relevant cost functions could then be considered, such as minimizing the deviation of the sound pressure level from its mean value [38], which could help flattening the acoustic frequency response.

If several electrodes are used, numerical simulations suggest that the optimization results could be improved by playing on the phase at which the different electrodes are actuated. One may imagine that the different electrodes could be excited with different amplitudes, and with arbitrary phase between each of them. The excitation of the different electrodes could also be frequency-dependent, and the optimization then becomes a combined filter design and modal control problem.

The large design freedom provided by the patterning of the electrodes of DE actuators still remains to be explored, and we believe accurate models of the dynamics of DE actuators may help investigating this path.

CRediT authorship contribution statement

Emil Garnell: Investigation, Writing - original draft. **Bekir Aksoy:** Investigation, Writing - review & editing. **Corinne Rouby:** Supervision, Writing - review & editing, Funding acquisition. **Herbert Shea:** Supervision, Writing - review & editing, Funding acquisition. **Olivier Doaré:** Conceptualization, Supervision, Writing - review & editing.

Declaration of Competing Interest

The authors declare that they have no known competing financial interests or personal relationships that could have appeared to influence the work reported in this paper.

Acknowledgements

The authors acknowledge the support of the French National Research Agency within the project SMArT (ANR-15-CE08-0007-02) and of the Swiss National Science Foundation, grant 200020_184661.

References

[1] Pelrine R, Kornbluh R, Pei Q, Joseph J. High-speed electrically actuated elastomers with strain greater than 100%. Science 2000;287(5454):836–9. https://doi.org/10.1126/science.287.5454.836.
[2] Goh YF, Akbari S, Khanh Vo TV, Koh SJA. Electrically-induced actuation of acrylic-based dielectric elastomers in excess of 500% strain. Soft Robot 2018;5 (6):675–84. https://doi.org/10.1089/soro.2017.0078.
[3] Suo Z. Theory of dielectric elastomers. Acta Mech Solida Sin 2010;23 (6):549–78. https://doi.org/10.1016/S0894-9166(11)60004-9.
[4] Hosoya N, Baba S, Maeda S. Hemispherical breathing mode speaker using a dielectric elastomer actuator. J Acoust Soc Am 2015;138(4):EL424–8. https://doi.org/10.1121/1.4934550.
[5] Rosset S, Gebbers P, O'Brien BM, Shea HR. The need for speed. In Electroactive Polymer Actuators and Devices (EAPAD) 2012, vol. 8340, International Society for Optics and Photonics, 2012, p. 834004.https://doi.org/10.1117/12.914623..
[6] Gu G, Zou J, Zhao R, Zhao X, Zhu X. Soft wall-climbing robots. Sci Robot 2018;3 (25):(Dec. https://doi.org/10.1126/scirobotics.aat2874.
[7] Chen Y, Zhao H, Mao J, Chirarattananon P, Helbling EF, Hyun N-SP, Clarke DR, Wood RJ. Controlled flight of a microrobot powered by soft artificial muscles. Nature 2019;575(7782):324–9. https://doi.org/10.1038/s41586-019-1737-7. url:https://doi.org/10.1038/s41586-019-1737-7.
[8] Duduta M, Hajiesmaili E, Zhao H, Wood RJ, Clarke DR. Realizing the potential of dielectric elastomer artificial muscles. Proc Natl Acad Sci 2019;116(7):2476–2481. arXiv:https://www.pnas.org/content/116/7/2476.full.pdf.https://doi.org/10.1073/pnas.1815053116..
[9] Loverich JJ, Kanno I, Kotera H. Concepts for a new class of all-polymer micropumps. Lab Chip 2006;6(9):1147–54. https://doi.org/10.1039/b605525g.
[10] Cao C, Gao X, Conn AT. A magnetically coupled dielectric elastomer pump for soft robotics. Adv Mater Technol 2019;4(8):1900128. https://doi.org/10.1002/admt.201900128.
[11] Lu Z, Shrestha M, Lau G-K. Electrically tunable and broader-band sound absorption by using micro-perforated dielectric elastomer actuator. Appl Phys Lett 2017;110(18). https://doi.org/10.1063/1.4982634. 182901.
[12] Keplinger C, Sun J-Y, Foo CC, Rothemund P, Whitesides GM, Suo Z. Stretchable, transparent, ionic conductors. Science 2013;341(6149):984–7. https://doi.org/10.1126/science.1240228.
[13] Conn AT, Rossiter J. Towards holonomic electro-elastomer actuators with six degrees of freedom. Smart Mater Struct 2012;21(3). https://doi.org/10.1088/0964-1726/21/3/035012. 035012.
[14] Zou Z, Li T, Qu S, Yu H. Active shape control and phase coexistence of dielectric elastomer membrane with patterned electrodes. J Appl Mech 2014;81(3). https://doi.org/10.1115/1.4025416. 031016.
[15] Langham J, Bense H, Barkley D. Modeling shape selection of buckled dielectric elastomers, arXiv preprint arXiv:1711.02602; 2017. arXiv:1711.02602..
[16] Anderson IA, Hale T, Gisby T, Inamura T, McKay T, O'Brien B, Walbran S, Calius EP. A thin membrane artificial muscle rotary motor. Appl Phys A 2010;98 (1):75–83. https://doi.org/10.1007/s00339-009-5434-5.
[17] Rosset S, Shea HR. Towards fast, reliable, and manufacturable DEAs: Miniaturized motor and Rupert the rolling robot. In SPIE Smart Structures and Materials + Nondestructive Evaluation and Health Monitoring, San Diego, California, United States, 2015, p. 943009.https://doi.org/10.1117/12.2085279..
[18] Hajiesmaili E, Clarke DR. Reconfigurable shape-morphing dielectric elastomers using spatially varying electric fields. Nat Commun 2019;10(1):183. https://doi.org/10.1038/s41467-018-08094-w.
[19] Shintake J, Cacucciolo V, Floreano D, Shea H. Soft robotic grippers. Adv Mater 2018;30(29):1707035. https://doi.org/10.1002/adma.201707035.
[20] Shintake J, Rosset S, Schubert B, Floreano D, Shea H. Versatile soft grippers with intrinsic electroadhesion based on multifunctional polymer actuators. Adv Mater 2016;28(2):231–8. https://doi.org/10.1002/adma.201504264.
[21] Gao X, Cao C, Guo J, Conn A. Elastic electroadhesion with rapid release by integrated resonant vibration. Adv Mater Technol 2019;4(1):1800378. https://doi.org/10.1002/admt.201800378.

[22] Zhu J, Cai S, Suo Z. Resonant behavior of a membrane of a dielectric elastomer. Int J Solids Struct 2010;47(24):3254–62. https://doi.org/10.1016/j.ijsolstr.2010.08.008.
[23] Fox JW, Goulbourne NC. Electric field-induced surface transformations and experimental dynamic characteristics of dielectric elastomer membranes. J Mech Phys Solids 2009;57(8):1417–35. https://doi.org/10.1016/j.jmps.2009.03.008.
[24] Clark RL, Fuller CR. Optimal placement of piezoelectric actuators and polyvinylidene fluoride error sensors in active structural acoustic control approaches. J Acoust Soc Am 1992;92(3):1521–33. https://doi.org/10.1121/1.403944.
[25] Doaré O, Kergourlay G, Sambuc C. Design of a circular clamped plate excited by a voice coil and piezoelectric patches used as a loudspeaker. J Vib Acoust 2013;135(5). https://doi.org/10.1115/1.4024215. 051025.
[26] Jiang CH, Kam TY, Chang YH. Sound radiation of panel-form loudspeaker using flat voice coil for excitation. Appl Acoust 2017;116:375–89. https://doi.org/10.1016/j.apacoust.2016.10.009.
[27] Keplinger C, Li T, Baumgartner R, Suo Z, Bauer S. Harnessing snap-through instability in soft dielectrics to achieve giant voltage-triggered deformation. Soft Matter 2012;8(2):285–8. https://doi.org/10.1039/C1SM06736B.
[28] Heydt R, Pelrine R, Joseph J, Eckerle J, Kornbluh R. Acoustical performance of an electrostrictive polymer film loudspeaker. J Acoust Soc Am 2000;107(2):833–9.
[29] Garnell E, Rouby C, Doaré O. Dynamics and sound radiation of a dielectric elastomer membrane. J Sound Vib 2019;459. https://doi.org/10.1016/j.jsv.2019.07.002. 114836.
[30] Garnell E, Doaré O, Rouby C. Coupled vibro-acoustic modeling of a dielectric elastomer loudspeaker. J Acoust Soc Am 2020;147(3):1812–21. https://doi.org/10.1121/10.0000930.
[31] Gent AN. A new constitutive relation for rubber. Rubber Chem Technol 1996;69(1):59–61. https://doi.org/10.5254/1.3538357.
[32] Hecht F. New development in freefem++. J Numer Math 2012;20(3–4):251–65. url:https://freefem.org/.
[33] Berenger J-P. A perfectly matched layer for the absorption of electromagnetic waves. J Comput Phys 1994;114(2):185–200. https://doi.org/10.1006/jcph.1994.1159.
[34] Doaré O, Garnell E, Rouby C. Radiation optimization of piezoelectric plates. Proceedings of ICA 2019, Aachen (Sep. 2019)..
[35] McCoul D, Hu W, Gao M, Mehta V, Pei Q. Recent advances in stretchable and transparent electronic materials. Adv Electron Mater 2016;2(5):1500407. https://doi.org/10.1002/aelm.201500407.
[36] Rosset S, Araromi OA, Schlatter S, Shea HR. Fabrication process of silicone-based dielectric elastomer actuators. J Visualized Exp 2016;108:(Feb. https://doi.org/10.3791/53423.
[37] Farina A. Simultaneous measurement of impulse response and distortion with a swept-sine technique. Audio Engineering Society Convention 108, Audio Engineering Society 2000.
[38] Lu G, Shen Y, Liu Z. Optimization of orthotropic distributed-mode loudspeaker using attached masses and multi-exciters. J Acoust Soc Am 2012;131(2):EL93–8. https://doi.org/10.1121/1.3672642.